Supplementary Online Information

Nanoparticle adhesion at liquid interfaces

Ke Sun[1], Yonas Gizaw[2], Halim Kusumaatmaja[3], and Kislon Voïtchovsky[1]**

1. *Department of Physics, Durham University, Durham, DH1 3LE, United Kingdom*
2. *GreenChemSolution, West Chester, OH 45069, United States of America*
3. *Institute for Multiscale Thermofluids, School of Engineering, The University of Edinburgh, Edinburgh, EH9 3FB, United Kingdom*

Correspondence: halim.kusumaatmaja@ed.ac.uk, kislon.voitchovsky@durham.ac.uk

Table of content:

1. Impact of tip velocity on the experimental force profiles

The quasistatic simulation model assumes the system to always be at equilibrium. To compare experimental measurements with the simulations, it is thus crucial to minimise (and ideally remove) any dynamical effect dependent on the tip moving velocity. Considering the travel distance of the tip inside the liquid (< 100 nm) and the velocities experimentally accessible (< 20 μm/s), inertial or viscosity effects are likely negligible. Instead, possible velocity dependence may arise from the movement of the contact line along the surface of the cantilever. We tested different tips and systematically varied operating velocities as exemplified in Fig. S1. The force profile depends on the tip velocity, but differences between curves become less important as the velocity decreases. Notably, the force profiles at velocities of 100 nm/s and 200 nm/s exhibited very similar characteristics, suggesting proximity to a quasistatic state. Consequently, we opted to systematically use the slowest velocity of 100 nm/s for comparison with the simulation results. Velocity-dependent effects can still not be excluded altogether, but the present strategy offers a good compromise between their minimisation while allowing for velocities high enough to avoid significant motion drift. Successful comparison with the simulation results (Fig. 3-4 in the main paper) confirms the suitability of this compromise.

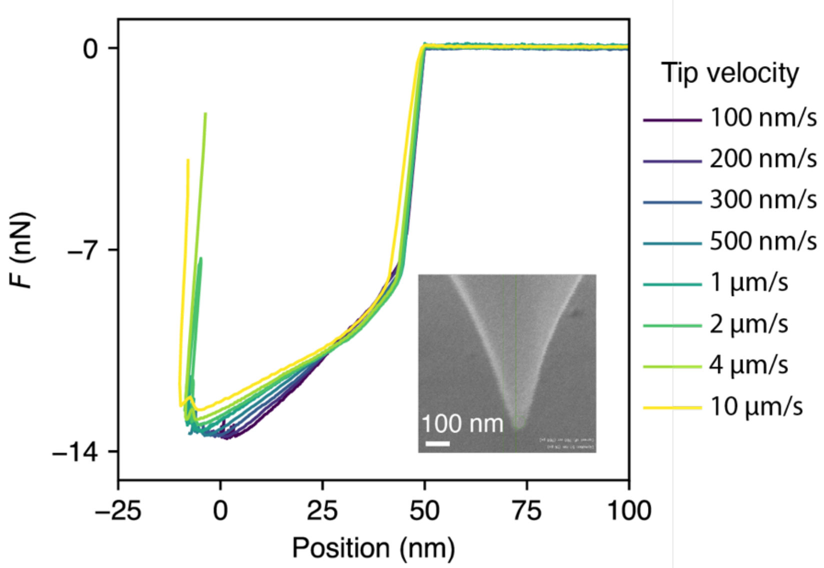

Figure S1: Example force curve acquired at different velocities (100 nm/s – 10 μm/s) in otherwise identical conditions. The curves were acquired with a same SPARK 70 tip (inset) and at a controlled temperature of 30.0 ± 0.1 °C.

2. Repeatability of the experimental measurements

To demonstrate the reproducibility of the experimental results, we repeated force spectroscopy measurements multiple times over an experiment with a given tip (Fig. S2). The curves all overlap well except for slight shifts along the position axis (left-most part of the curves). This is due to the indentation depth of the tip in the liquid varying by up to a nanometre between consecutive measurements. This evolution is likely due to molecules of the liquid (oil) partly remaining at the surface of the tip after the rupture of the capillary bridge. Consistently, the changes occur immediately after initial contact with the liquid, but as the experiment progresses, all the force curves fully overlap. The average force curve (red line) serves as the displayed force profile for this particle adhesion.

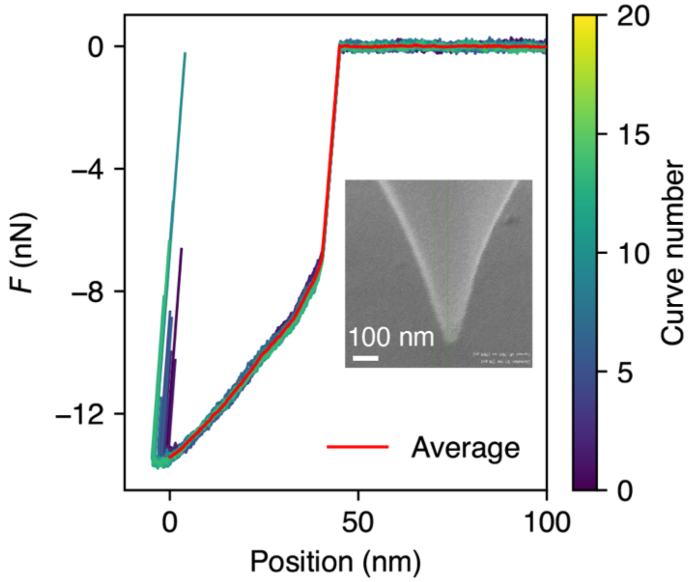

Figure S2: Multiple repeats of experimental force curve measurements taken consecutively with a same tip. The curves are aligned at the rupture point of the capillary bridge. The good overlap of the curves near the rupture point indicates full reproducibility of the measurements. The red line represents the average. The tip employed in the measurements is the same Spark 70 tip used in Fig. S1.

3. Contact angle measurements

The contact angle measurements of silicone oil on representative tip surfaces were performed in both air and water to replicate the experimental conditions. In ambient air, a 3 μL droplet of 10 cSt silicone oil was deposited on either a platinum film or a silicon wafer. On both the platinum film and silicon wafer, the silicone oil spread towards the edges, exhibiting near-complete wetting approaching contact angle $\theta \sim 0°$, see Fig. S3. In water, due to the density difference between the silicone oil and water, a drop of silicone oil was deposited from below onto a platinum film immersed in a water bath. The measured contact angle was $\theta = 106.8 \pm 3.7°$, determined using the drop shape analysis LBADSA fitting method in ImageJ (Fig. S4).[1,2]

The platinum film used to represent the AFM tip surfaces has an intrinsic roughness significantly larger than that of the tip on the scale of the contact angle measurement. While addressing nanoscale roughness on the actual tip surfaces is not feasible, the measured contact angle on the platinum film can be corrected by the Wenzel model:[3]

$$\cos\theta_m = \cos\theta_Y \times r$$

where θ_m is the measured contact angle, θ_Y is the corrected Young's contact angle, and r is roughness ratio, defined as the ratio between the actual surface area and the projected area (r >1 for rough surfaces). The roughness ratio was determined by topography imaging using JPK NanoWizard V BioScience AFM (Bruker, USA), followed by triangulation of the measured surfaces to calculate the actual surface area, yielding $r = 1.015 \pm 0.006$. After correction, the contact angle in water remains

$\theta \sim 0°$, while in air, the corrected contact angle is $\theta = 106.5 \pm 3.8°$. The contact angles do not show significant difference when considering surface roughness.

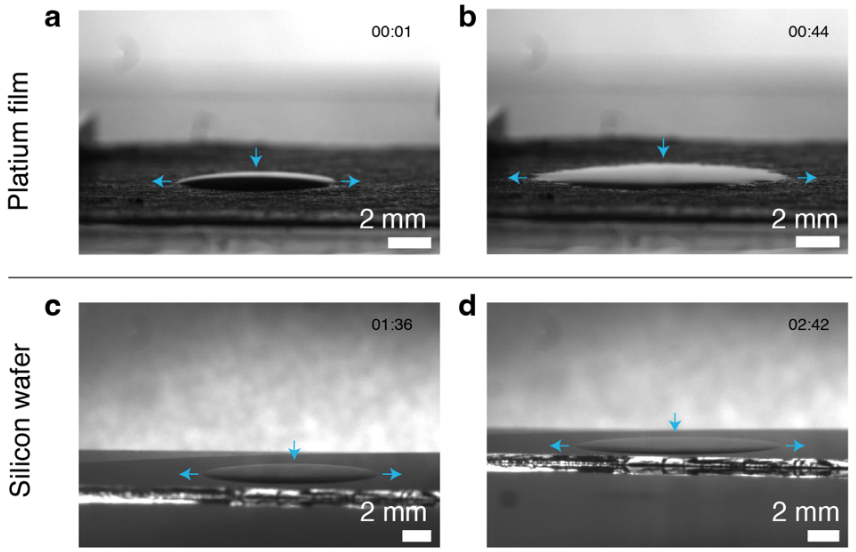

Figure S3: Spreading dynamics of the silicone oil on platinum film and silicon wafer in air, demonstrating near-complete wetting $\theta \sim 0°$ on both surfaces on longer timescales. After deposition, the droplets spread uniformly as shown in **(a)** and **(c),** and eventually spread towards the edges to fully wet the surfaces, as shown in **(b)** and **(d)**. Arrows in the figures highlight the edges of the droplet for better visualisation. The time stamps are shown in the top right corner of each figure in the format of mm:ss.

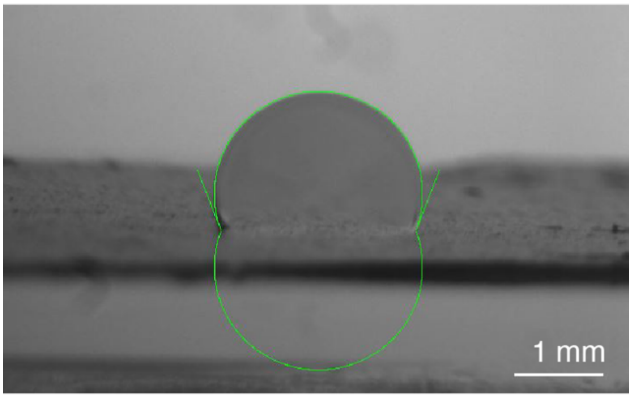

Figure S4: Example of contact angle measurement of 10 cSt silicone oil on platinum film surrounded by ultrapure water. Due to the density difference, the measurement was performed by immersing a glass slide coated with platinum film in ultrapure water and injecting a drop of silicone oil from below. The image is flipped horizontally. The droplet was fitted by drop shape analysis LBADSA method (green line), resulting in a measured contact angle of $\theta = 106.8 \pm 3.7°$ based on three repeat measurements.

4. Example Surface Evolver script

An example script ***example.fe*** is provided as a separate file in Supplementary Information.

5. Processing of the AFM Data

The experimental data was processed by a Python script to obtain force versus tip-sample position results. Firstly, the raw deflection photodetector signal $P_v(V)$ was converted to cantilever deflection $Z_c(m)$: $Z_c = P_v \times sensitivity$. The piezo position Z_p was adjusted to the actual tip position relative to the sample surface through a bending correction, using separation $= Z_c + Z_p$. Finally, the force F was calculated from Hooke's law: $F = k \times Z_c$, where k is the spring constant.

In some of the measurements (e.g. an experiment using JPK NanoWizard 3 with a Scout 70 Nu Nano tip, Fig. S5), a combination of practical experimental factors made it difficult to remove the tip oscillations from the measured static tip deflection (Fig. S5a). This is a problem for particularly soft cantilevers with low resonance frequencies. To address the issue, a filtering approach based on the Fast Fourier Transform (FFT) was built into our analysis script: in a typical force curve containing high-frequency noise (Fig. S5a), taking the extension part as an example, the force signal was decomposed into constituent frequency components using the FFT (Fig. S5b, yellow line). A sigmoid filter function: $y = 1/(1 + \exp(-\beta(\alpha - x)))$ (Fig. S5c) was then applied to eliminate high-frequency noise. The parameters α and β govern the midpoint and the decreasing rate of the function, respectively. Both parameters were tailored specifically to experimental values, ensuring an appropriate filtering. The filtered low-frequency signal can then be restored to the original force data through the Inverse Fast Fourier Transform (IFFT) (Fig. S5d). This protocol was applied to force curves exhibiting high-frequency noise, generating a clean set of force curve data with all characteristic features preserved.

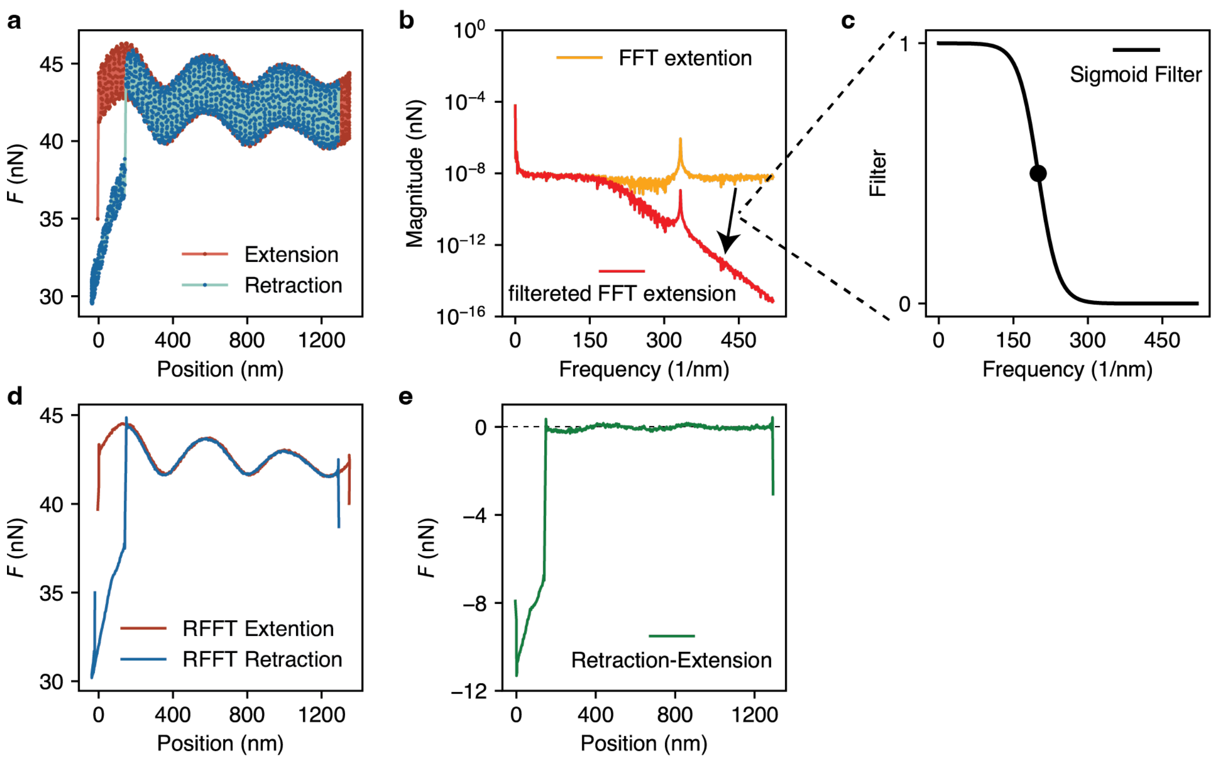

Figure S5: Example data processing for deflection curves with unwanted periodic noise. The original experimental data **(a)** exhibits the high-frequency oscillations of the cantilevers as well as low frequency optical interferences. The Fourier Transform for the extension data **(b)** reveals a clear peak for the higher frequency oscillations that can be removed using a sigmoid low-pass filter **(c)**. Taking the Inverse Fourier Transform of the filtered data **(d)** shows that the high-frequency noise has indeed been removed. Further subtraction of the retraction curve from the extension curve **(e)** yields a suitable force profile for comparison with the simulations.

In the final step, the low-frequency laser interference was removed by subtracting the retraction curve from the extension curve (Fig. S5e). This laser interference arises from constructive interference between the laser reflection from the cantilever and the light scattered by the sample surface. Following this protocol, the features of the force curve are preserved to the greatest extent.

6 Impact of tip truncation on the capillary rupture point

In experimental measurements, controlling the shape of the tip apex is challenging regardless of the degree of control on the cone angle. At the point of rupture, the capillary bridge is attached precisely to the apex region of the tip, likely dominating the rupture process. To better reflect this situation, most simulations in this work were conducted with a truncated conical tip. While a simplification, it reflects the finite size and inherent imperfections of the experimental apex. Beyond this, it offers an opportunity to investigate numerically the impact of the truncation on the resulting force profile.

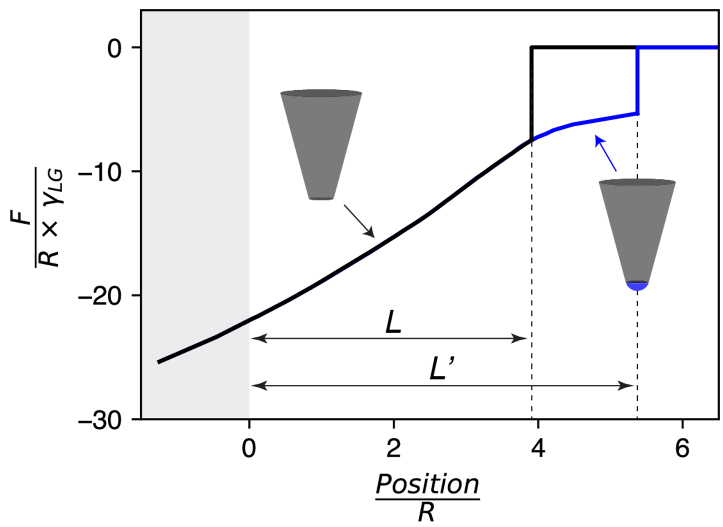

Figure S6: Simulated force profiles for different truncated tips. Inset: cartoon illustrations of the two conical tips: one with a smooth spherical end and the other with a sharp truncation. The maximum length of the capillary bridge before rupture is labelled as *L'* for the spherical-end cone and *L* for the sharp-truncated cone. These lengths are determined with the position x = 0 being the point of contact between the tip end and the liquid interface. The simulations were initialised with the tip partially immersed in the liquid (grey-shaded area) and proceeded by evolving the interface between each step of tip withdrawal from the liquid's surface. The force profile of the sharp-truncated cone is shown by the black line, while the force profile of the spherical-ended cone is in blue line. The two profiles overlap at positions where *Position/R < 3.9*. Both axes are normalised with end radius *R* and liquid-gas surface tension γ_{LG} to be unitless.

Here, two tips are set up with identical overall cone shapes, but with either a sharp truncation or a smooth transition to a spherical end. Fig. S6 shows simulations run comparatively for these two geometries, referred to as 'sharp-truncated' (black line) and 'spherical-end' (blue line). Initially, when the three-phase contact line is on the conical section, both models exhibited the same profile. However, when the contact line reaches the end of the conical section, the behaviour diverges: for the sharp-truncated cone, the liquid detached from the tip, and the capillary bridge ruptured. In contrast, for the spherical-end tip, the contact angle continued to slide along the spherical part. Consequently, the capillary bridge ruptured at different positions, with the maximum capillary bridge length *L'* for the spherical-end cone greater than *L* for the sharp-truncated cone. This comparison suggests that the details of the particle truncation may be at the origin of the discrepancy in rupture point between experiments and simulations (see main text Fig. 3).

Aside from the details of truncation geometry, it is worth noting that the normalisation process used to compare directly the experimental and simulated curves affects the apparent non-monotonic dependence of the capillary bridge length on the cone angle α. The simulations employ cones truncated at the same height, resulting in different end radii, *R,* which are used as the characteristic length in the normalisation (Fig. S7a). In Fig. S7b, the raw simulation data (prior to normalisation) show that *L* increases monotonically with *α*. However, after normalisation (Fig. S7c, same as Fig. 4 of the main text), *L/R* exhibits a non-monotonic behaviour due to the variation in end radius R, across cone angles. In addition, when considering *L* across both experimental and simulation contexts, variations in apex features can further contribute to differences in capillary bridge length, as noted previously above.

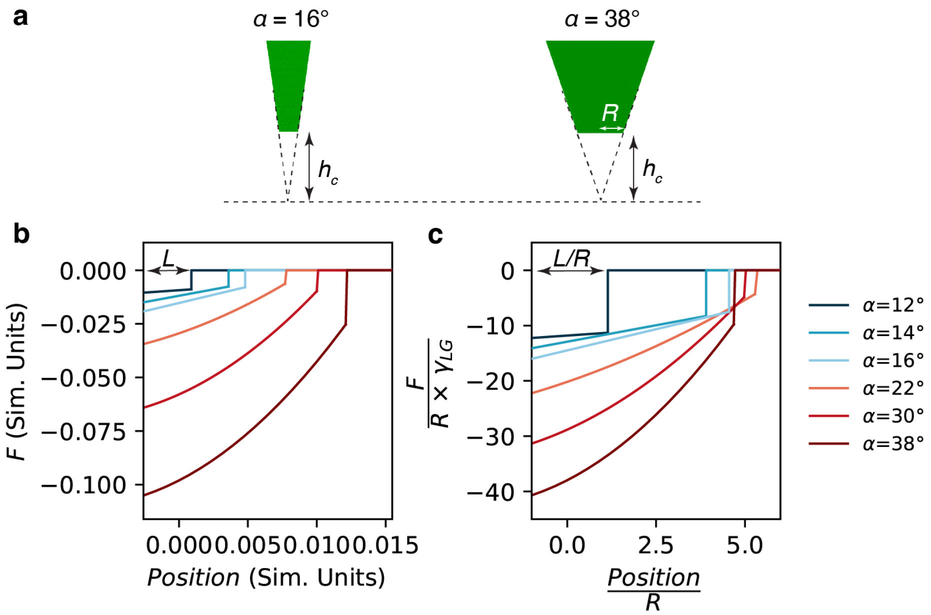

Figure S7. **(a)** Schematic illustration of narrow and wide cones used in the simulation model, where *α* represents the cone angle. Both cones were truncated at the same height, h_c, resulting in different end radii, *R*. **(b-c)** Simulation force profiles for cones with varying *α*: before normalisation **(b)** and after normalisation by end radius and surface tension **(c)**. *L* denotes the capillary bridge length. *L/R* denotes the normalised capillary bridge length.

7. Non-axisymmetric conical geometry

Although axisymmetric by design, the tip used for the data presented in Fig. 5 presents some imperfections, with its cone angle depending on the viewpoint from which the electron microscopy measurements are taken, as illustrated in Fig. S8.

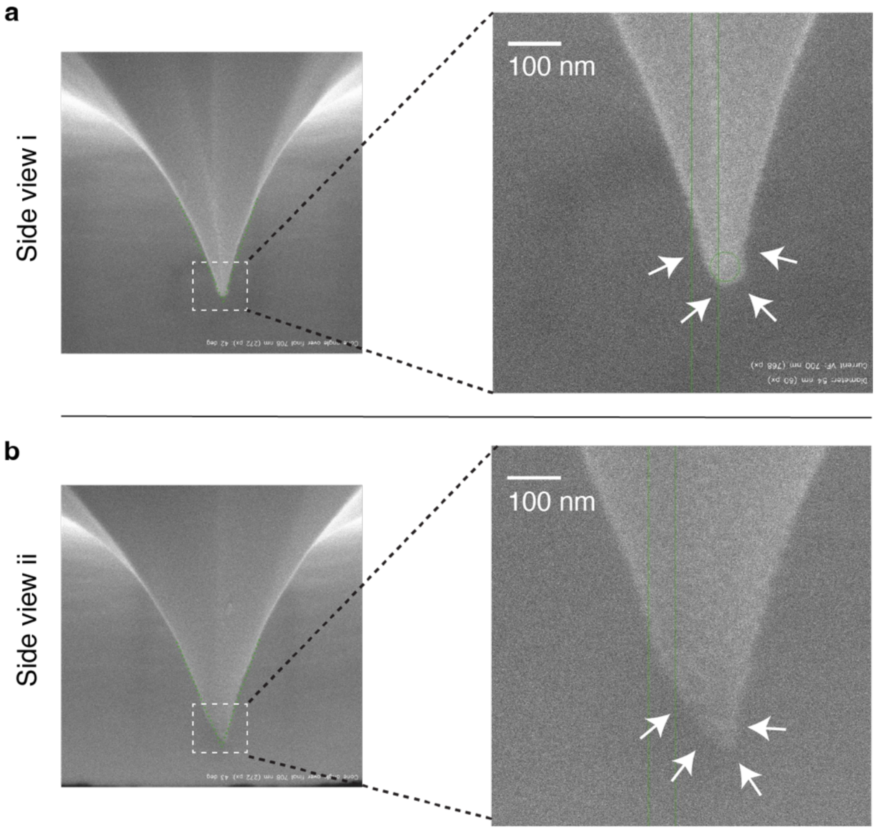

Figure S8: Electron microscopy images for the tip used for the air-oil and water-oil interface measurements (Fig. 5). Images taken with different side views illustrate a typical tip imperfection with geometrical variations between different viewpoints. **(a)** The tip is observed to be relatively symmetric with a slightly rounded shape at the apex from side view i. This view was used to measure the geometrical characteristics for Fig. 5. **(b)** The tip shows asymmetry from side view ii, with a noticeable cone angle change at the apex. Apex features are highlighted by white arrows to aid visualisation.

8. Changes in interfacial energies as a function of the contact angle θ

When increasing the contact angle, the force profile changes significantly during particle withdrawal: the solid-fluid interfacial area increases while the solid-liquid area decreases until reaching zero when the three phase contact line reach the tip apex end. The behaviour of the liquid-fluid interfacial area is more complex: it may either decrease or increase depending on the contact angle and the position of the contact line. To better understand the changes in the different contributions of the interfacial free energies, here we illustrate the typical behaviours for three different contact angles, $\theta = 30°$, $75°$ and $100°$. The interfacial energy profile can be divided into two parts for analysis depending on whether the contact line (i) slides along the conical particle, or (ii) is pinned at the apex edge of the particle (Fig. S9).

- At $\theta = 30°$, the liquid builds up a large capillary meniscus due to strong wetting on the solid surface. During withdrawal, the three-phase contact line slides along the solid cone, leading to a decrease in solid-liquid and liquid-fluid energies, and an increase in the solid-fluid energy. When the contact line reaches the edges of the sharp-truncated conical particle, it becomes pinned, causing a slight increase in liquid-fluid energy during over the additional steps of withdrawal. Eventually, the capillary bridge ruptures.

- At $\theta = 75°$, the tendency for the solid-liquid and solid-fluid energies is similar, but the liquid-fluid interfacial energy initially increases. The contact line reaches the apex edges midway through the withdraw process, followed by strong pinning due to the more comparable wetting properties of the liquid and the fluid on the solid. The liquid-fluid contribution increases more sharply than before the contact line is pinned.
- At $\theta = 100°$, before the contact line meets the apex, the meniscus is considerably smaller due to the similar affinities of the fluid and liquid for the solid particle. The energy profile is primarily governed by an increase in liquid-fluid energy after the contact line reaches the apex edges.

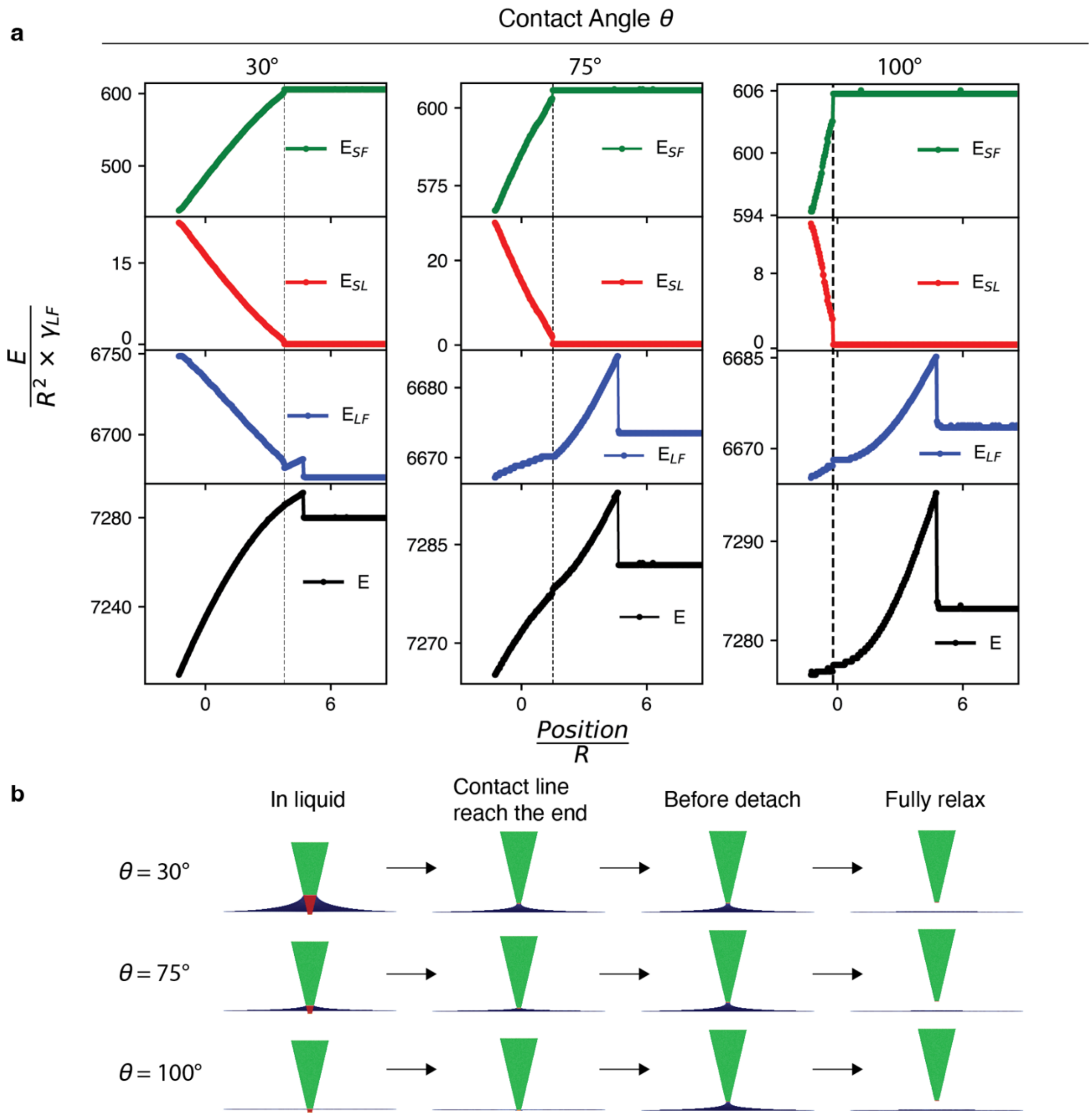

Figure S9: (a) Energy contributions from the different interfaces in the three-phase system, simulated for different contact angles. In simulation, we set the interfacial tensions γ_{LF}:γ_{SF}:$\gamma_{SL} = 1$:1:$(1 - \cos(\theta))$, with L, S and F standing for liquid, solid and surrounding fluid, respectively. The total energy for each interface is simply $E = \gamma \times A$, with A is the area of the interface considered. E_{SF}, E_{SL}, and E_{LF} are the interfacial energy from the three interfaces, respectively. E is the overall energy in the simulation system. Note that all energies are normalised by $R^2 \times \gamma_{LF}$ to be unitless, and the position axis is normalised by R.The dash line represents the tip position where the three-phase contact line reached the edge of the tip apex and pinned there until fully detachment. **(b)** Simulation snapshots (clip view) during tip particle withdrawal from the liquid interface. Initially, the tip particle is immersed within the liquid interface. As it withdraws, the three-phase contact line moves along the particle's side wall until it reaches the particle's apex, where it becomes pinned before the particle fully detaches.

Overall, these results suggest that when the contact angle increases, the energy profile transitions from being mainly governed by the sliding of the contact line along the particle to the relaxation of the liquid-fluid interface after the contact line reaches the apex end.

9. Sqone normalisation

Varying the shape factor s systematically allows us to explore the geometry across from cone to pyramid. Given the end shape of sqone deviates from a perfectly symmetric circle, we used both the end radius *R* and the effective end radius *R'* to examine the effect of the normalisation factor. The effective apex radius *R'* was obtained by calculating the perimeter of the particle apex and converting it into the equivalent circular radius (Fig. S10a). The normalised force profiles show that the maximum adhesion force F_{AD} always increases with the increase of the shape factor *s*, regardless of the choice of normalisation (Fig. S10b-c). However, the maximum capillary bridge length *L* differs based on the normalisation method: when normalised by *R*, *L/R* remains constant (Fig. S10b), whereas when normalised by *R'*, *L/R'* decreases as the shape factor *s* increases (Fig. S10c). This indicates that *L* can vary depending on the characteristic length used for normalisation, which may also contribute to the discrepancies observed in the results section when comparing experimental and simulation data (Fig. 3).

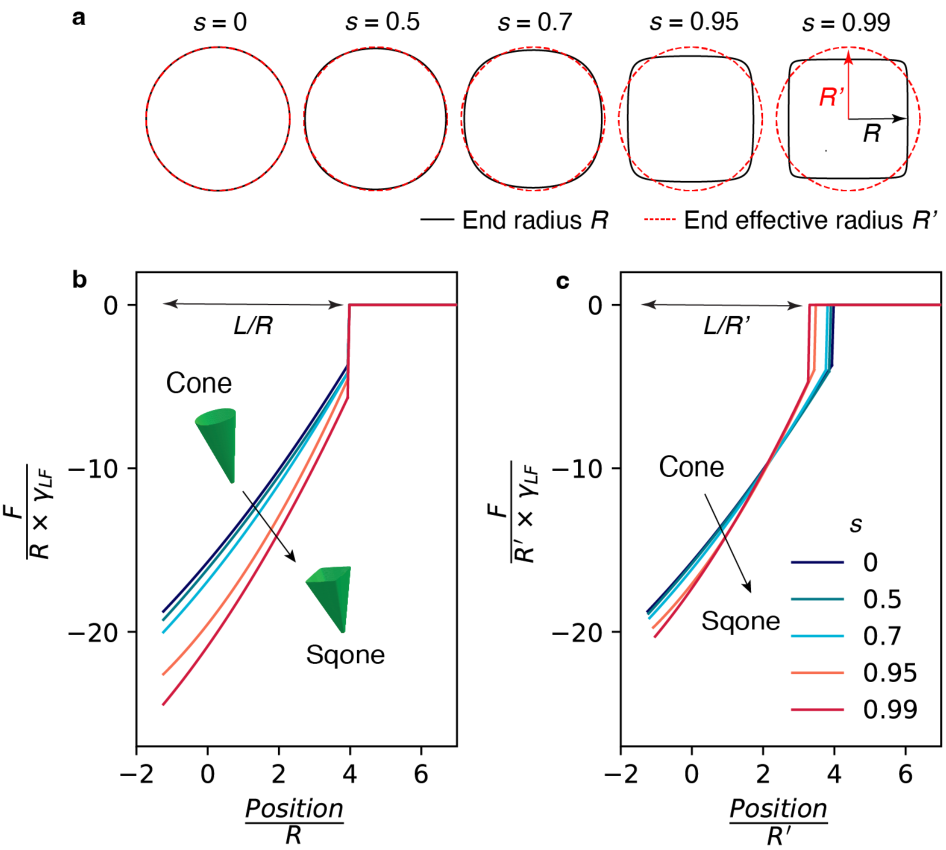

Figure S10: Simulation force profiles with varied shape factor *s*. **(a)** The end cross-sectional shape of the particle, with end radius *R* and the effective end radius *R'*. *R'* is determined by the perimeter of the particle apex. **(b)** and **(c)** show different choices of characteristic length for normalisation: **(b)** employs end radius *R*, while **(c)** employs effective end radius *R'*. *L/R* and *L/R'* represent the normalised maximum capillary bridge length before rupture.

10. References

1 C. A. Schneider, W. S. Rasband and K. W. Eliceiri, *Nat. Methods*, 2012, **9**, 671–675.
2 A. F. Stalder, T. Melchior, M. Müller, D. Sage, T. Blu and M. Unser, *Colloids Surf. Physicochem. Eng. Asp.*, 2010, **364**, 72–81.
3 R. N. Wenzel, *Ind. Eng. Chem.*, 1936, **28**, 988–994.